Oxidation of Metals (2021) 96:105–116
https://doi.org/10.1007/s11085-021-10054-7

ORIGINAL PAPER

Corrosion Behavior of Cr-Containing Alloys under Cyclic Reaction in Wet CO_2 Gas at 650°C

Xuteng Xi[1] · Jianqiang Zhang[1] · David John Young[1]

Received: 1 June 2021 / Revised: 1 June 2021 / Accepted: 7 June 2021 /
Published online: 22 July 2021
© The Author(s), under exclusive licence to Springer Science+Business Media, LLC, part of Springer Nature 2021

Abstract

The corrosion behavior of seven commercial alloys (602CA, 310SS, 253MA, 800H, F321, F316L, 304SS) was investigated in a wet CO_2 gas under cyclic reactions up to 150 cycles at 650°C. Water vapor accelerated the oxidation of all alloys. Alloy 602CA was alumina-forming in dry CO_2 but changed to chromia-forming in the wet gas. In wet gas, the 310SS and 253MA underwent breakaway oxidation which was enhanced by the cyclic reaction. Spallation and buckling of the outer iron oxide scale were considerable for the less-protective alloys, 800H, F321, F316L and 304SS, with the formation of reddish iron oxide whiskers on the scale surface. The carburisation of F321, F316L and 304SS was identified and found to be reduced significantly by the presence of water vapor. The effect of water vapor on oxidation, carburisation, oxide buckling and whisker formation is discussed in comparison with that in dry gas.

Keywords Austenitic alloys · Cyclic reaction · Wet CO_2 · High-temperature corrosion

✉ Jianqiang Zhang
j.q.zhang@unsw.edu.au

Xuteng Xi
xuteng.xi@unsw.edu.au

David John Young
d.young@unsw.edu.au

[1] School of Materials Science and Engineering, University of New South Wales, Sydney, NSW 2052, Australia

Introduction

Oxyfuel combustion is a promising technology to reduce CO_2 emissions in fossil fuel fired power plants, where the flue gas contains mainly CO_2 and H_2O [1]. However, this CO_2-rich gas has been found to be extremely corrosive at elevated temperatures. Low-alloy steels and ferritic-martensitic alloys are therefore unable to survive, and austenitic alloys are needed because of their higher creep-rupture strength and oxidation resistance [2].

Thermal cycles are normally encountered in industrial application and found to accelerate the corrosion of alloys. Austenitic alloys might be more susceptible to thermal-cyclic reaction, owing to their significantly higher thermal expansion coefficients than those of ferritic/martensitic steels [3]. A preliminary study found that the cyclic reaction accelerated the formation of iron-rich nodules for high-chromium-containing austenitic alloys in dry CO_2 [4]. As the atmosphere related to oxyfuel combustion always contains H_2O, it is necessary to determine the role of water vapor on the corrosion behaviors of austenitic alloys in CO_2 under cyclic reaction conditions.

Experimental Details

Total seven commercial alloys were tested in this work, including 602CA, 310SS, 253MA, 800H, F321, F316, 304SS. Their compositions are shown in Table 1 where 602CA is a nickel base alloy, and all others are iron base austenitic steels. Rectangular shaped sample coupons were cut, ground and then electro-polished. The electropolishing method was applied to remove the surface deformation zone created during sample preparation. Details about sample preparation are described elsewhere [4].

All specimens were reacted in a vertical furnace under atmospheric pressure with a linear gas flow rate of 1.5 cm/s in Ar-20CO_2-20H_2O (volume percentage). Cyclic condition was accomplished with the movement of vertical furnace, for 60 min in heating zone at 650°C and 15 min in furnace cooling zone at about 150°C, for up to 150 cycles. Isothermal corrosion experiments for 310 h were also carried out for purposes of comparison.

Weight changes of oxidized samples were measured immediately after cooling of the furnace by an analytical balance (Mettler Toledo XP205) with an accuracy

Table 1 Chemical compositions of tested commercial alloys (all in wt.%)

	602CA	310SS	253MA	304SS	F321	F316L	800H
Fe	9.4	Bal	Bal	Bal	Bal	Bal	Bal
Cr	25.7	24–26	21	18	17–19	16–18	20.7
Ni	Bal	19–22	11	8	9–12	10–14	30.4
Others	2.2 Al	1.5 Si, 2 Mn	1.6 Si	2 Mn	1 Si, 2 Mn	1 Si, 2 Mn, 2 Mo	0.5 Si, 0.7 Mn

of 0.01 mg. Oxide phases produced by exposure were identified by X-ray diffraction (XRD; Empyrean I) with Cu-Kα radiation. Metallographic observation was carried out by optical microscopy (OM), scanning electron microscopy (SEM; Hitachi S3400X) with energy dispersive X-ray spectroscopy (EDS; Bruker). Some selected samples were further analyzed by transmission electron microscopy (TEM; CM200). The TEM samples were prepared by Focused Ion Beam milling (FIB; FEI xT Nova Nanolab 200). Etchant of Murakami's solution (2g $K_3Fe(CN)_6$ + 2 g KOH + 20 ml H_2O) was used to reveal carbides formed in reacted samples.

Results

Isothermal Reaction in Wet Carbon Dioxide

Weight Change

Figure 1 compares the weight changes of alloys after 310 h exposure to Ar-20CO_2 and Ar-20CO_2-20H_2O. All the 3 more protective alloys (602CA, 310SS, 253MA) identified in dry gas [4] showed obvious weight increases when water vapor was added to the gas mixture (Fig. 1a). Among them, the 602CA alloy had the least weight increase, 0.02 mg/cm^2 in dry gas and 0.08 mg/cm^2 in wet gas. For the other two alloys, 310SS and 253MA, distinct weight changes were visible in wet gas, especially for 253MA alloy. No weight losses were observed for these three alloys, which is however the situation for all other alloys (Fig. 1b).

For F321, F316L and 304SS, their weight changes went into negative in both gas atmospheres, which indicates the spallation of oxide scales after oxidation. For 800H, a slight weight loss was recorded in dry gas, while there was an apparent weight gain (2.11mg/cm^2) after 310 h oxidation in wet gas.

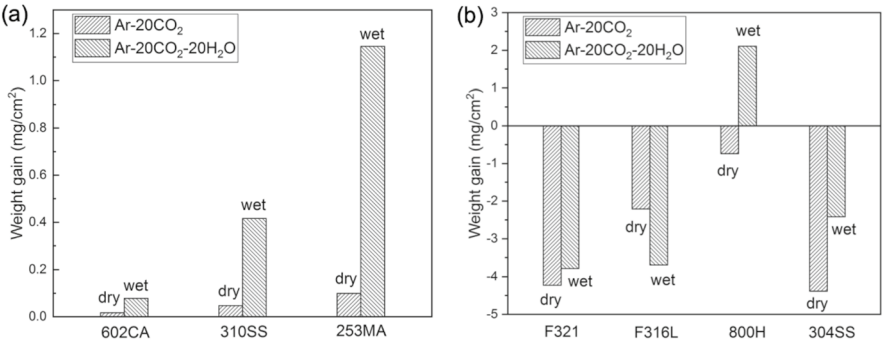

Fig. 1 Weight changes of **a** more protective alloys and **b** less-protective alloys after 310 h oxidation in Ar-20CO_2 and Ar-20CO_2-20H_2O at 650°C

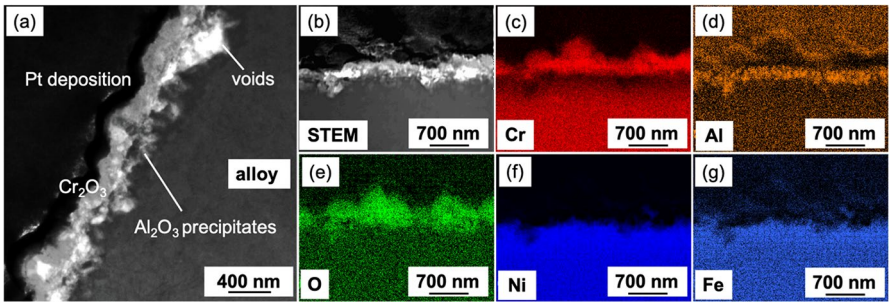

Fig. 2 TEM/EDX analyses of thin scales formed on 602CA after 310 h oxidation in Ar-20CO_2-20H_2O at 650 °C: **a** bright field TEM and **b** STEM images with **c–g** area mapping of the scale (K_α for all elements)

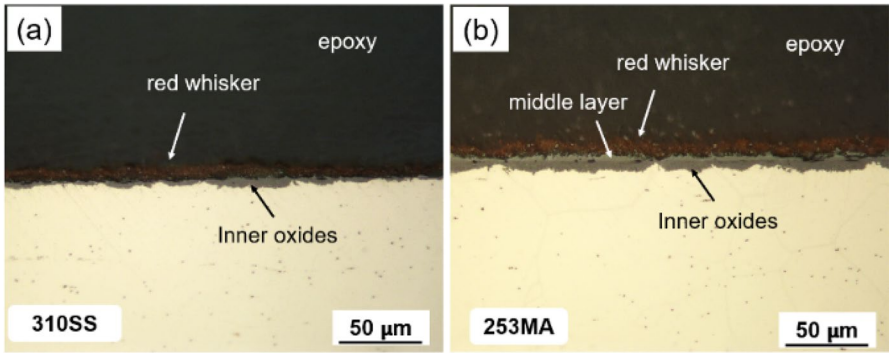

Fig. 3 Metallographic cross-sections of **a** 310SS and **b** 253MA reacted in Ar-20CO_2-20H_2O for 310 h at 650°C

Cross-section Analysis

After 310 h oxidation in wet gas, an ultra-thin oxide layer was formed on 602CA. The bright field TEM cross-section (Fig. 2) of this alloy showed that a thin chromia scale formed on top of the alloy surface, with some voids underneath. The chromia layer is not uniform with an average thickness of 190nm ± 80nm. Underneath the chromia layer, large quantities of alumina precipitates grew near the interface (Fig. 2a). The EDS area mapping further confirmed above reaction products (Fig. 2c–g).

The cross-sections of 310SS and 253MA after reaction in wet gas are shown in Fig. 3. In dry gas, a thin and uniform chromia scale formed for both alloys [4]. However, in wet gas they experienced certain extents of attack during 310 h reaction. The growth of outer red whisker was observed for both alloys. For 310SS, the inner oxide layer was shallow and non-uniform, but for 253MA, the inward growth of inner layer was more uniform, although it could be hindered at grain boundaries. Between red whisker and inner oxide layer, a middle layer existed for 253MA (Fig. 3b).

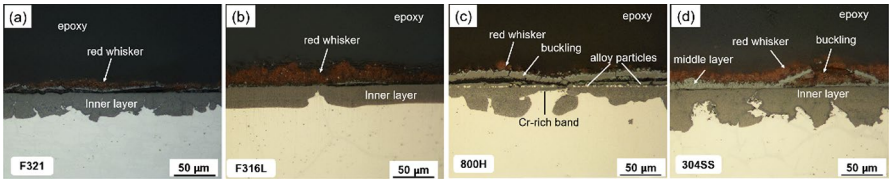

Fig. 4 Metallographic cross-sections of **a** F321, **b** F316L, **c** 800H, **d** 304SS after 310 h oxidation in Ar-20CO_2-20H_2O

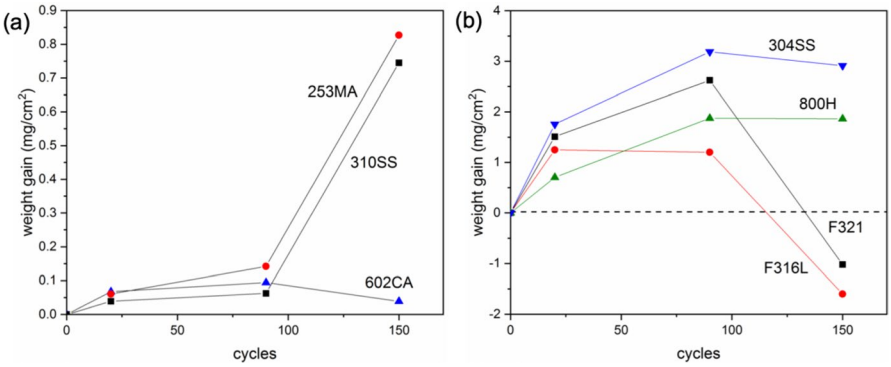

Fig. 5 Weight gain kinetics of **a** more protective alloys and **b** less-protective alloys during cyclic reaction in Ar-20CO_2-20H_2O

Cross-sections of the other less-protective alloys after reaction in wet gas are shown in Fig. 4. All these alloys formed outer and inner oxide layer. In general, severe spallation and buckling of the outer oxide layer were observed, and the growth of reddish whisker was found on the top of the oxide scale. A rather thick and uneven inner oxide layer was formed inside the alloy below the original metal surface. For 800H, noticeable alloy particles were deposited at the interface of inner and outer oxide layer, forming a discontinuous line structure (Fig. 4c).

Cyclic Reaction in Wet Carbon Dioxide

Weight Gain Kinetics

Weigh gain kinetics during cyclic reaction in wet gas are plotted for low weight gains of group 1 alloys (602CA, 310SS and 253MA) in Fig. 5a and high weight gains of group 2 alloys (F321, F316L, 800H and 304SS) in Fig. 5b. In the first group, the weight gains of 602CA were the lowest. The value of weight gain was only 0.04mg/cm^2 after 150 cycles of the reaction. For 310SS and 253MA, although weigh gains were very low at low cycles, after 150-cycles reaction, the weight gains increased to 0.73 and 0.83 mg/cm^2, respectively. For the alloys in group 2, weight gains were noticeable after only 20-cycles reaction. After 90 cycles, F321, 800H and 304SS

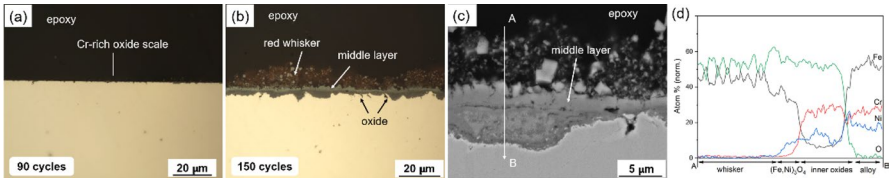

Fig. 6 Metallographic cross-sections of 310SS after reaction in Ar-20CO_2-20H_2O for **a** 90 cycles, **b** 150 cycles, **c** BSE-image after 150 cycles and **d** corresponding line-scan analysis

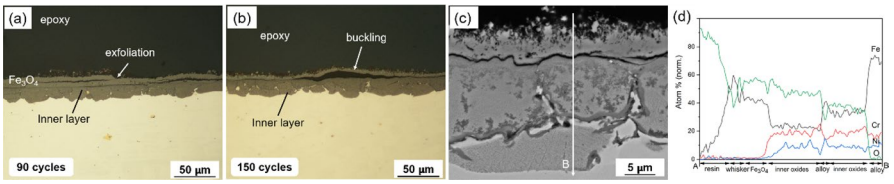

Fig. 7 Metallographic cross-sections of F321 after reaction in Ar-20CO_2-20H_2O for **a** 90 cycles, **b** 150 cycles, **c** BSE-image after 150 cycles and **d** corresponding line-scan analysis

developed greater weight increases (2.62 mg/cm^2, 1.87 mg/cm^2, 3.1 mg/cm^2 respectively). In contrast, F316L lost weight from 1.25 to 1.20 mg/cm^2. After 150 cycles, both F321 and F316L underwent weight loss, indicating severe oxide spallation. A minor weight gain was observed for 800H, and 304SS had a slight weight loss.

Cross-section Analysis

Figures 6a and b show cross-sections of 310SS after 90-cycles and 150-cycles reactions. After 90-cycles exposure, generally the surface was covered with a thin scale, but some small pitting had developed. After 150 cycles, the reddish whiskers were well developed above the middle layer, forming an outer oxide scale, and an inner oxide layer grew below (Fig. 6b). Higher magnification SEM image (Fig. 6c) revealed that the outermost whisker zone was porous and embedded in the epoxy mount, so the oxygen concentration oscillated within the whisker area. These whiskers are iron oxides, as confirmed by EDS and Raman analysis (not shown). The EDX line-scan (Fig. 6d) revealed the presence of Ni, together with the dominant Fe and O, in the middle layer, suggesting it could contain (Fe, Ni)$_3O_4$. The enrichment of Cr and the presence of Ni and Fe in the inner oxide indicated the presence of Cr-containing spinel, (Fe, Cr, Ni)$_3O_4$.

The oxidation behavior of 253MA alloy during cyclic reaction in wet gas was similar to that of 310SS. Only a few oxide nodules were generated on the sample surface after 90 cycles reaction, but by 150 cycles, uniform outer and inner oxide layers had developed.

After 90 cycles reaction, F321 alloy had formed a thick outer Fe_3O_4 scale, identified by Raman Spectroscopy (not shown), and a deep inner oxide layer (Fig. 7). Cracking and exfoliation of the outer Fe_3O_4 scale are illustrated in Fig. 7a. After 150-cycles reaction, the spalling of outer layers was severe, and only fragments

remained. Buckling of the outer layer was captured in Fig. 7b. With increasing cycles, the depth of inner oxide increased where some alloy matrix metal was incorporated. The BSE-image in Fig. 7c, clearly shows a band of metal rich in Ni and Fe between two inner oxide regions (Fig. 7c). Above this metallic layer, a chromium-enriched band developed along grain boundaries.

Both F316L and 304SS developed the same oxide layer constitutions as F321 after 90 and 150 cycles. Spalling and buckling of the outer oxide scale were also observed at 150 cycles (not shown).

Cross-sections of 800H after 150 cycles reaction are shown in Fig. 8. Multiple oxide layers were developed during oxidation. The EDX mapping results (Figs. 8b–e) revealed that the outermost two buckling layers were iron oxide. The well-attached middle oxide layer contained Fe and Ni and some Ni-rich particles had been incorporated into this layer. The inner oxide layer contained Fe, Ni, Cr and O.

Carburisation in Wet Carbon Dioxide

The carbides formed in the samples after 150-cycles exposure were revealed by etching with the Murakami's reagent. The results showed that carburization did occur by forming carbides when alloys were oxidized in Ar-20CO_2-20H_2O at 650°C. Alloys (602CA, 310SS, 253MA, 800H) after annealing in Ar-5H_2 gas for 150 h at 650°C generated carbide precipitants at all grain boundaries in the whole cross-section. Therefore, additional carbide formation, if any, due to the gas reaction cannot be clearly identified for these alloys [4]. However, after annealing in Ar-5H_2 at 650°C, alloys F321, F316L and 304SS also showed carbide formation, but with much less density. After reaction in Ar-20CO_2-20H_2O, the newly formed carbides due to the gas reaction can be clearly distinguished because of an increased density and amount, as shown in Fig. 9.

The results for 304SS demonstrated increased carbides along grain boundaries near the alloy surface after exposure to Ar-20CO_2-20H_2O. The density of carbides immediately below the inner oxide layer was higher than that in interior parts of the alloy (Fig. 9). Similar occurrence of increased carbide formation was also observed for F321 alloy after reaction in the wet CO_2 gas.

Figure 10 compares the carbon penetration of F316L after reaction in dry and wet gas for 90 and 150 cycles. The carburization due to gas reaction was evidenced in both atmospheres. In dry gases, the average depth of carbon penetration increased from around 275 µm after 90 cycles to 387 µm after 150 cycles. But in wet gas, this depth was only 93 µm after 90 cycles reaction and 235 µm after 150-cycles reaction.

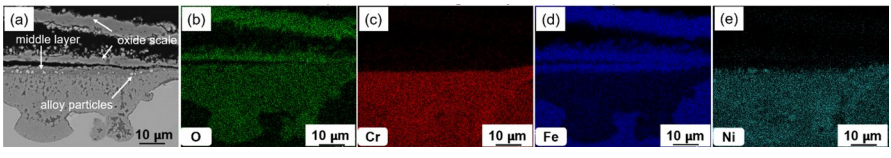

Fig. 8 **a** BSE-image of 800H after reaction in Ar-20CO_2-20H_2O for 150 cycles and **b–e** EDS mapping

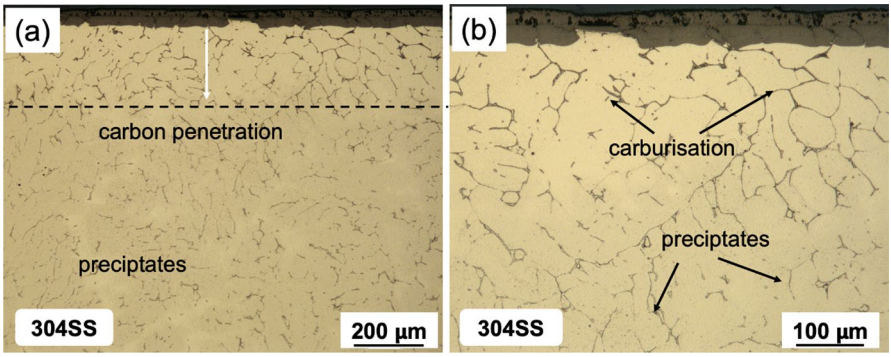

Fig. 9 Metallographic cross-sections of 304SS **a** at low magnification, **b** at higher magnification after 150-cycles of reaction in Ar-20CO_2-20H_2O (etched in Murakami's solution to reveal carbides)

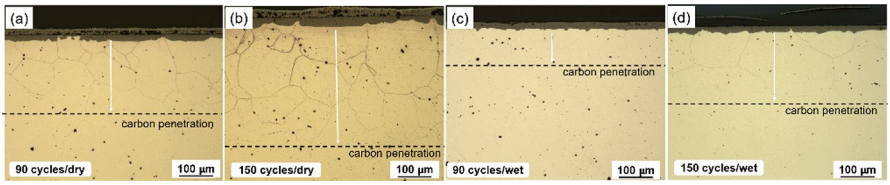

Fig. 10 Metallographic cross-sections of F316L after reaction in Ar-20CO_2 for **a** 90 cycles, **b** 150 cycles and after reaction in Ar-20CO_2-20H_2O for **c** 90 cycles and **d** 150 cycles

Similar comparisons of cross-sections of F321 and 304SS after exposure in both atmospheres also showed the decreased extent of carburization in wet gas. This alleviating effect of water vapor on carburization in CO_2-rich gases appears to be general for low chromium content stainless steels.

Discussion

The addition of water vapor had a significant influence on corrosion performance of these austenitic alloys and changed their oxide morphologies. It changed the oxide structure of 602CA from alumina-forming in dry CO_2 (a thin and uniform alumina scale with scattered chromium oxide [4]) to chromia-forming in wet gas (thin chromia scale with alumina precipitates underneath, Fig. 2). Water vapor also accelerated corrosion of 310SS and 253MA in CO_2, by increasing weight gains and forming iron-rich oxide layers. The less-protective alloys, F321, F316L, 800H and 304SS, all went into breakaway oxidation in both dry and wet conditions but the oxide morphology was different: buckling of outer scales and formation of iron-rich oxide whiskers prevailed after exposure in the wet gas. Carburisation was found after exposure in both gases along grain boundaries of alloys, but slower carburization was observed in the wet CO_2 gas. The discussion will focus on the effects of water vapor on oxidation and carburisation of austenitic alloys; the development of buckling and the mechanism of whisker growth in the wet gas will also be discussed.

Water Vapor Effect on Oxidation

For Ni-base 602CA, the results showed that water vapor transformed this alloy from alumina-forming to chromia-forming [4]. To understand this, Wagner's theory was used to determine the critical Cr concentration $N_{Cr}^{(1)}$ (mole fraction) to change from internal to external oxidation [5].

$$N_{\mathrm{Cr}}^{(1)} = \left(\frac{\pi g}{2v} \frac{V_m}{V_{\mathrm{Cr}O_v}} \frac{N_O^{(S)} D_O}{\tilde{D}_{\mathrm{Cr}}} \right)^{\frac{1}{2}} \tag{1}$$

Here g is a critical volume fraction of oxide precipitates, v the stoichiometric coefficient of CrO_v (1.5), V_i the molar volume of the alloy or the oxide, $N_O^{(S)} D_O$ the oxygen permeability in the alloy, $\tilde{D}_{\mathrm{Cr}}$ the alloy inter-diffusion coefficient. The calculation was performed for dry CO_2 gas in our previous paper [4], and $N_{\mathrm{Cr}}^{(1)}$ was found to be 0.31, indicating that 602CA $\left(N_{\mathrm{Cr}} = 0.29\right)$ cannot form outer chromia layer at 650°C. The critical level of aluminum for the formation of alumina scale was also taken into account by using Wagner's theory. The result was $N_{\mathrm{Al}}^{(1)} = 0.38$ [4], predicting that a continuous external Al_2O_3 scale could not form on the alloy surface either. This prediction was not in agreement with the experimental observation that a thin uniform alumina sale did form after 310 h oxidation in dry CO_2 gas. This discordance can be rationalized by the beneficial effect of chromium for the formation of protective alumina scale [6].

The formation of outer chromia scale in wet CO_2 gas indicates that the $N_{\mathrm{Cr}}^{(1)}$ was reduced to a lower level that the Cr concentration in 602CA $\left(N_{\mathrm{Cr}} = 0.29\right)$ meets the new critical value. It is further speculated that the function of $\frac{N_O^{(S)} D_O}{\tilde{D}_{\mathrm{Cr}}}$ might be affected by water vapor because of the interactions of H_2O with scale or alloy. For Ni and Ni-base alloy with low Fe, it was reported that water vapor had little effect on oxygen permeability [7]. It was recently reported for Ni–Cr alloys that the effective oxygen permeability $N_O^{(S)} D_O^{\mathrm{eff}}$ was decreased in wet CO_2 compared with that in dry CO_2, but this discrepancy was reduced for higher Cr level alloys [8]. Thus a decrease in $\frac{N_O^{(S)} D_O}{\tilde{D}_{\mathrm{Cr}}}$ would be expected, and therefore a lower value of $N_{\mathrm{Cr}}^{(1)}$.

The detrimental effect of water vapor on iron-based alloys was well revealed by the rapid oxidation of 310SS and 253MA in Ar-20CO_2-20H_2O. Both of them did not passivate in wet gases by forming iron-rich oxide scale after exposure in both isothermal and cyclic reaction. However, in dry CO_2, the partially protective chromia scale was formed even after long time exposure, together with thermally induced break of the chromia scale and formation of oxide nodules. As observed from cross-sections after early 90-cycles reaction, 310SS remained protective with some pitting along grain boundaries (Fig. 6a), 253MA also showed partially protective area of thin scale. The transition from initial protective to non-protective after long time reaction indicates that chromia scale did form at the start of oxidation, but fail to retain it, that means that $N_{\mathrm{Cr}}^{(1)}$ could be satisfied but these two alloys fail to meet the second critical Cr level $N_{\mathrm{Cr}}^{(2)}$ for maintaining Cr_2O_3 growth [9].

$$N_{\mathrm{Cr}}^{(2)} = \frac{V_m}{V_{\mathrm{CrO}_{1.5}}} \left(\frac{\pi k_p}{2\tilde{D}_{\mathrm{Cr}}} \right)^{\frac{1}{2}} \tag{2}$$

where k_p is the parabolic rate constant for chromia scale thickening. Unfortunately, the thickening kinetics of chromia layer in 310SS and 253MA were not obtained after early exposure, and after long time exposure, their surfaces were covered with Fe-rich sale, and no chromia scale was observed. Therefore, no detailed value can be obtained for $N_{\mathrm{Cr}}^{(2)}$.

Oxide Buckling

Oxide buckling was frequently observed on samples after reaction in water-containing environment. In dry gases, the cracking and spallation of outer oxide scale were found after immediate cooling in isothermal reaction or during cyclic reaction, which was attributed to thermal stress developed at scale/alloy interfaces. With the addition of water vapor, the failure of scale adherence was still noticeable, but the formation of scale buckling was frequently observed, which showed different morphology from that in dry gas (Fig. 4).

Several literatures reported the phenomenon of buckling in water-containing atmosphere. For austenitic steels, this buckling was found in Fe_3O_4 layer or at the interface of Fe_3O_4/alloy [10]. The buckling of internal oxidation zone (IOZ) in Ni–Cr alloys in wet CO_2 was also reported [8], and it was rationalized by the enhanced inward oxygen transport in wet CO_2 gas, resulting in an increased volume expansion of IOZ and following buckling.

In this paper, as the scale buckling was observed in both isothermal reaction (Figs. 4c, d) and thermal-cyclic reaction (Figs. 7, 8), it could be deduced that this phenomenon is not originated from thermal-induced stress and should result from growth stress of outer scales in this study. While many voids developed among Fe_3O_4 layer in dry gas [4], it is found that dense and uniform outer layers with less voids were formed for alloys exposed to wet gas at the relatively early cycles (Fig. 7a), indicating mixed transport of iron and oxygen happened and probably inward transport of oxygen dominated for the wet gas. With more oxides formed at the interface of outer and inner oxide layers, the growth stress could be built up at the interface and initiate the buckling there.

Another mechanism of buckling formation is that the water vapor lowers the adherence of scales and facilitates the propagation of flaw in the scale. This negative effect of water vapor was reported for austenitic steel oxidized in pure steam where chromia scale underwent cracking and buckling [11]. The originality of cracking and buckling was attributed to the formation of hydrogen molecules and hydrogen defects under chromia layer. For iron-rich scale, it is assumed that gas molecules could be transported directly into scales [12], producing oxygen and hydrogen. Thus, the existence of H–O bond or hydrogen is also possible in the iron-rich scale, facilitating the flaw propagation.

Whisker Formation

The formation of reddish iron oxide whiskers on sample surface was found in water-containing atmosphere but not in dry CO_2 gases. Cyclic reaction accelerated this whisker formation for 310SS and 253MA, in comparison with that in isothermal reaction. However, for all other non-protective alloys with thick oxide scale formation, the whisker formation is significant and independent of isothermal or cyclic condition.

The whisker formation on metal surface has been discussed extensively in many works. The chromia whisker was observed on pure chromium after exposure to Ar/H_2/H_2O, and it was attributed to the fast diffusion of Cr and catalytic dissociation of H_2O molecules at the whisker tips [13]. The formation of chromia whisker was reported to be promoted by the addition of water vapor in Fe–Cr and Fe–Cr-Ni model alloys [14]. The whisker formation was also found in iron as α-Fe_2O_3. Crystallographic studies revealed that bladelike whiskers or blades consist of twinned oxide crystals. It is believed that the oxide grows from internal transport of iron to tips along twin interfaces where the diffusion of iron was faster than oxygen [15]. Water vapor would prompt the formation of whiskers significantly. It was proposed that the dissociation of H_2O molecules would be the limiting step in terms of whisker formation [16].

The formation of reddish iron oxide whisker could also be regarded as a way to release compressive stress [10]. The growth stress in outer oxide layer was enhanced to a large extent with the addition of water vapor as obvious buckling formation was found in this work, corresponding well with the formation of whiskers. The stress-driven grain boundary diffusion with rapid diffusion of cations was reported for nanowires CuO formation during oxidation of Cu [17], which could be the part of reason for iron oxide whisker formation.

Carburisation

Carburisation occurred in both dry and wet CO_2 gases, but clearly the depth of carburization zone was decreased in wet gas, compared with that in dry gas (Fig. 10). The addition of water vapor almost has no change in the carbon activity of the gas, 7.7×10^{-16} for Ar-20CO_2-20H_2O and 1.6×10^{-15} for Ar-20CO_2. One possible mechanism is the competitive absorption of oxidants [18]. It was reported that carbon penetrates via oxide grain boundaries. In addition to carbon, other oxidants, e.g., H_2O, sulfur, could also diffuse inwards along oxide grain boundary. The sequences of preferential absorption on oxide is $H_2O > CO > H_2 > N_2$ [18]. Thus water vapor would preferentially occupy the active site of grain boundary and reduce the rate of carbon diffusion and therefore carburisation. This mechanism explains the experimental results qualitatively.

Conclusions

Seven commercial alloys, one nickel base and six iron base austenitics, were exposed isothermally and cyclically to Ar-20CO_2-20H_2O at 650°C. According to weight gain kinetics, these alloys can be classified in two groups, one with small weight gain

(602CA, 310SS and 253MA) and the other with thick oxide and apparent scale spallation (non-protective) (F321, F316L, 800H and 304SS).

Water vapor changed oxide morphologies significantly. The alumina scale formed on 602CA in dry gas was changed to a chromia scale in the presence of water vapor in the gas, and some alumina precipitates were found underneath the chromia scale after 310 h reaction. For 310SS and 253MA, water vapor accelerated breakaway oxidation, generating uniform iron-rich oxide layers in both isothermal and cyclic reaction. Any effect of cyclic reaction was not significant, due to the overwhelming water vapor effect.

For non-protective alloys (F321, F316L, 800H and 304SS), buckling of Fe_3O_4 scale was observed which is attributed to the release of compressive growth stress developed during magnetite layer formation in the H_2O-containing atmosphere. In addition, reddish iron oxide whiskers on the surface were generated on the base Fe_3O_4 due to the fast diffusion of iron and the rapid dissociation of H_2O molecules.

Carburisation was identified for alloys F321, F316L and 304SS with an increased intergranular carbide density after reaction in both atmospheres. Water vapor slowed carburisation considerably. The penetration depths of carburisation were decreased for F321, F316L and 304SS in wet gases due to the co-existence of carbon and water vapor derived species in oxide grain boundaries, which slows inward carbon diffusion and therefore alloy carburisation.

Acknowledgements The authors would like to thank Australian Research Council for financial support of this project under the Discovery project scheme.

References

1. Buhre, B.J.P., et al., Progress in Energy and Combustion Science, 2005. **31**: p. 283.
2. Powell, C.A. and B.D. Morreale, MRS Bulletin, 2008. **33**: p. 309.
3. Viswanathan, R., J. Sarver, and J.M. Tanzosh, Journal of Materials Engineering and Performance, 2006. **15**: p. 255.
4. Xi, X., C. Kong, and J. Zhang, Oxidation of Metals, 2019.
5. Wagner, C., Zeitschrift für Elektrochemie, 1959. **63**: p. 772.
6. Airiskallio, E., et al., Corrosion Science, 2010. **52**: p. 3394.
7. Prillieux, A., et al., Oxidation of Metals, 2017. **87**: p. 273.
8. Xie, Y., J. Zhang, and D.J. Young, Corrosion Science, 2018. **136**: p. 311.
9. Wagner, C., Journal of the Electrochemical Society, 1952. **99**: p. 369.
10. Olszewski, T., Vol. 159. 2012: Forschungszentrum Jülich.
11. Yuan, J., et al., Corrosion Science, 2016. **109**: p. 36.
12. Ehlers, J., et al., Corrosion science, 2006. **48**: p. 3428.
13. Hänsel, M., W.J. Quadakkers, and D.J. Young, Oxidation of Metals, 2003. **59**: p. 285.
14. Nguyen, T.D., J. Zhang, and D. Young, Corrosion Science, 2015. **83**.
15. Tollman, R.L. and E.A. Gulbransen, Journal of The Electrochemical Society, 1968. **115**: p. 770.
16. Raynaud, G.M. and R.A. Rapp, Oxidation of Metals, 1984. **21**: p. 89.
17. Yuan, L., et al., Acta Materialia, 2011. **59**: p. 2491.
18. Anghel, C., et al., Applied Surface Science, 2004. **233**: p. 392.

Publisher's Note Springer Nature remains neutral with regard to jurisdictional claims in published maps and institutional affiliations.